CrossMark click for updates

Local and global structural drivers for the photoactivation of the orange carotenoid protein

Sayan Gupta[a,1], Miklos Guttman[b,1], Ryan L. Leverenz[c], Kulyash Zhumadilova[d], Emily G. Pawlowski[c], Christopher J. Petzold[a], Kelly K. Lee[b], Corie Y. Ralston[a], and Cheryl A. Kerfeld[a,c,e,f,2]

[a]Physical Biosciences Division, Lawrence Berkeley National Laboratory, Berkeley, CA 94720; [b]Department of Medicinal Chemistry, University of Washington, Seattle, WA 98195; [c]Department of Energy Plant Research Laboratory, Michigan State University, East Lansing, MI 48824; [d]School of Science and Technology, Nazarbayev University, Astana 010000, Kazakhstan; [e]Department of Plant and Microbial Biology, University of California, Berkeley, CA 94720; and [f]Department of Biochemistry and Molecular Biology, Michigan State University, East Lansing, MI 48824

Edited by Robert Haselkorn, University of Chicago, Chicago, IL, and approved August 21, 2015 (received for review June 27, 2015)

Photoprotective mechanisms are of fundamental importance for the survival of photosynthetic organisms. In cyanobacteria, the orange carotenoid protein (OCP), when activated by intense blue light, binds to the light-harvesting antenna and triggers the dissipation of excess captured light energy. Using a combination of small angle X-ray scattering (SAXS), X-ray hydroxyl radical footprinting, circular dichroism, and H/D exchange mass spectrometry, we identified both the local and global structural changes in the OCP upon photoactivation. SAXS and H/D exchange data showed that global tertiary structural changes, including complete domain dissociation, occur upon photoactivation, but with alteration of secondary structure confined to only the N terminus of the OCP. Microsecond radiolytic labeling identified rearrangement of the H-bonding network associated with conserved residues and structural water molecules. Collectively, these data provide experimental evidence for an ensemble of local and global structural changes, upon activation of the OCP, that are essential for photoprotection.

orange carotenoid protein | photoprotection | X-ray footprinting | hydrogen deuterium exchange | SAXS

Photosynthetic organisms have evolved a protective mechanism known as nonphotochemical quenching (NPQ) to dissipate excess energy, thereby preventing oxidative damage under high light conditions (1). In plants and algae, NPQ involves pH-induced conformation changes in membrane-embedded protein complexes and enzymatic interconversion of carotenoids (2, 3). Cyanobacteria, in contrast, use a relatively simple NPQ mechanism governed by the water soluble orange carotenoid protein (OCP). The OCP is composed of an all α-helical N-terminal domain (NTD) consisting of two discontinuous four-helix bundles and a mixed α/β C-terminal domain (CTD), which is a member of the widely distributed nuclear transport factor 2-like superfamily (Fig. S1*A*) (4, 5). There are two regions of interaction between the NTD and CTD (4, 5): the major interface, which buries 1,722 Å of surface area, and the interaction between the N-terminal alpha-helix (αA) and the CTD (minor interface) (Fig. S1*A*). A single noncovalently bound keto-carotenoid [e.g., echinenone (ECN)] spans both domains in the structure of the resting (inactive) form of the protein (OCP^O).

The NTD and CTD of the OCP have discrete functions. The isolated NTD acts as an effector domain that binds to the antenna whereas the CTD has been proposed to play a sensory/regulatory role in controlling the OCP's photoprotective function (6). Exposure to blue light converts OCP^O to the active (red) form, OCP^R (7). OCP^R is involved in protein–protein interactions with the phycobilisome (PB) (5) and the fluorescence recovery protein (FRP), which converts OCP^R back to OCP^O (8). The OCP^R form is therefore central to the photoprotective mechanism, and determining the exact structural changes that accompany its formation are critical for a complete mechanistic understanding of the reversible quenching process in cyanobacteria. Although crystal structures exist of both the (inactive) OCP^O (4, 5) and the active NTD (effector domain) form of the protein (9), crystallization of the activated, full-length OCP^R has not been achieved. To identify the protein structural changes that occur after absorption of light by the OCP's ECN chromophore, we undertook a hybrid approach to structurally characterize OCP^R in solution.

In *Synechocystis* OCP^O, the 4-keto group on the "β1" ring of ECN is H-bonded to two conserved residues, Y201 and W288, in a hydrophobic pocket in the core of the CTD (Fig. S1*B*) (5). The other end of the carotenoid is positioned between the two four-helix bundles of the NTD. Several conserved residues within 3.9 Å of the carotenoid are known to interact with its extensive conjugation and result in fine tuning of the spectral characteristics of the OCP (Fig. S1*B*) (4, 5); these residues have been implicated in photochemical function via mutagenesis studies (5). A recent study of the OCP bound to the carotenoid canthaxanthin (OCP-CAN) showed that photoactivation of the OCP results in a substantial translocation (12 Å) of the carotenoid deeper into the NTD (9). Mutational analyses of the full-length OCP and biochemical studies on the constitutively active NTD [commonly known as the red carotenoid protein (RCP)] suggested that the NTD and CTD at least partially separate, resulting in the breakage of an interdomain salt-bridge (R155–E244) upon photoactivation (9–12). Together, the previous studies suggest that large-scale protein structural changes in the OCP accompany carotenoid translocation upon light activation; however, such changes in the context of the full-length protein have yet to be experimentally demonstrated. Here, we report use of X-ray radiolytic labeling

Significance

The orange carotenoid protein (OCP) is critical for the antenna-associated energy-dissipation mechanism of cyanobacteria under high light conditions. We show that light activation causes a global conformation change, the complete separation of the two domains of the OCP. Such a conformational change has been postulated to be a prerequisite for interaction with the antenna. We also identify local structural changes in residue solvent accessibility and roles for structural water molecules in activation of the OCP. By combining small-angle scattering, hydrogen-deuterium exchange, and X-ray hydroxyl radical footprinting studies, we were able to construct a model of the structural changes during the activation of the OCP with an unprecedented level of detail.

Author contributions: S.G., M.G., R.L.L., K.K.L., C.Y.R., and C.A.K. designed research; S.G., M.G., R.L.L., K.Z., E.G.P., and C.J.P. performed research; S.G., M.G., R.L.L., and E.G.P. contributed new reagents/analytic tools; S.G., M.G., R.L.L., C.Y.R., and C.A.K. analyzed data; and S.G., M.G., R.L.L., K.K.L., C.Y.R., and C.A.K. wrote the paper.

The authors declare no conflict of interest.

This article is a PNAS Direct Submission.

See Commentary on page 12547.

[1]S.G. and M.G. contributed equally to this work.

[2]To whom correspondence should be addressed. Email: ckerfeld@lbl.gov.

This article contains supporting information online at www.pnas.org/lookup/suppl/doi:10.1073/pnas.1512240112/-/DCSupplemental.

with mass spectrometry (XF-MS) and hydrogen/deuterium exchange with mass spectrometry (HDX-MS), which detect residue-specific changes (13–15), to investigate the structural changes that occur during OCP photoactivation. In conjunction with small angle X-ray scattering (SAXS), which enables characterization of global conformational changes in the solution state (16), we show that dissociation of the NTD and CTD is complete in photoactivated OCP. This separation is accompanied by an unfolding of the N-terminal α-helix that is associated with the CTD in the resting state. We also pinpoint changes in specific amino acids and structurally conserved water molecules, providing insight into the signal propagation pathway from carotenoid to protein surface upon photoactivation. Collectively, these data provide a comprehensive view of both global and local intraprotein structural changes in the OCP upon photoactivation that are essential to a mechanistic understanding of cyanobacterial NPQ.

Results and Discussion

Global Structural Changes upon Photoactivation of the OCP as Observed by SEC, CD, and SAXS. Size-exclusion chromatography (SEC) of purified OCP^O [*Synechocystis* OCP containing ECN (OCP-ECN)] in darkness yielded a single (nearly Gaussian) peak in its chromatogram (Fig. S2*A*). An ∼1:1 ratio of the 470:496-nm absorbance in the peak is consistent with the UV-visible spectrum of OCP^O (7). Relative to globular standards, the estimated molecular mass (MW) of OCP^O is 36 kDa (Fig. S2*A*), consistent with the expected monomeric MW (35.4 kDa). In contrast, SEC of OCP preilluminated with blue light (OCP^R) yielded a heterogeneous elution profile with an additional peak eluting before the OCP^O monomer peak (Fig. S2*B*). The A470:496 ratio (<<1) of the early eluting peak is consistent with the visible absorbance spectrum of OCP^R (7), and its relative elution volume (corresponding to a predicted globular mass of 63 kDa) suggests a larger size (Stokes radius) for OCP^R. Similar results were obtained in the buffer used for XF- and HDX-MS studies (20 mM phosphate, pH 7.4, 100 mM NaCl).

Light scattering was used to examine whether the larger apparent size of OCP^R was resulting from a change in the oligomeric state (i.e., dimerization). Dynamic light scattering, a metric dependent on the protein's shape, showed a 10% increase in the radius of hydration of the OCP upon activation (Table S1). At the same time, the static light scattering intensity, a shape-independent metric, did not change, indicating no change in the MW of the protein. Therefore, structural changes within the monomer, and not changes in the oligomeric state, were responsible for the altered elution time observed by analytical SEC.

Circular dichroism (CD) spectroscopy was used to determine whether secondary structure changes contributed to the larger size of OCP^R. Only small differences in the far-UV (185–260 nm) CD spectra are apparent after illumination of OCP (Fig. S2*C*). The small difference between the OCP^O and OCP^R spectra was found to be consistently reproducible across multiple independent measurements (Fig. S2*D*), and careful monitoring of the time-dependent CD signal and sample absorbance ensured that data were collected on the OCP^R form without significant contribution from OCP^O (Fig. S2 *E* and *F*). Three different algorithms (CDSSTR, CONTINLL, and SELCON3) were used to calculate the predicted secondary structure of OCP^O and OCP^R from the experimental CD curves (Table S2) (17). The helical (47.0%), beta strand (13.2%), turn (17.1%), and unordered (22.8%) content of OCP^O predicted by the average of the results from all methods is in good agreement with the crystal structure (48.3% helix, 15.9% strand, 14.6% turn, 21.2% unordered). For OCP^R, all three algorithms predict a small decrease (∼2%) in α-helical content and a small increase (∼1%) in disordered structure (Table S3). A small increase in beta-strand content (∼1–3%) is predicted using the CDSSTR and CONTINLL methods, but not SELCON3. Overall, these results are consistent with the loss of only a small portion of the protein's α-helical structure (2% α-helical content = ∼6 residues) after illumination, with the majority of the secondary structure remaining otherwise unchanged.

To obtain more detailed information on the changes in tertiary structure that occur during the transition to the light activated state OCP^R, we used tandem SEC-SAXS with online illumination of the eluting OCP (Fig. S3*A*). This experimental configuration enabled us to circumvent sample aggregation and vary light intensity to obtain datasets with different levels of illumination (*SI Methods*). The SAXS patterns of the OCP with and without illumination are shown in Fig. 1*A*. With illumination, there is a distinct change in the scattering pattern, most apparent between q = 0.1–0.2. The radius of gyration data from Guinier and real space (GNOM) analysis indicated a large difference in the global structure, with OCP^R showing a ∼30% and ∼50% increase in the radius of gyration (Rg) and maximal dimension (D_{max}), respectively (Table S4). Kratky plots for both the OCP^O and OCP^R converged near baseline, indicating that, although there are large global changes, the protein remains folded (Fig. 1*B*) (16). The real space pairwise distance distribution [P(r)] plot showed that, whereas OCP^O has a profile consistent with a globular protein, OCP^R is much more elongated (Fig. 1*C*).

Native mass spectrometry has shown that the OCP^O forms dimers, which are also consistently observed in crystal structures (4, 5), and a change in the monomer/dimer distribution upon activation (18). By SAXS, the scattering intensity at zero angle, I(0), is the same for OCP^O and OCP^R (775 ± 6 and 785 ± 8, respectively), indicating no difference in the MW of the protein (Table S4). We used SAXSMOW (19), a method for determination of the MW of globular proteins from the raw SAXS data, which resulted in an estimate of ∼38.2 kDa for the OCP. The contrast to previous studies may be due to weak dimerization that is observed only at higher protein concentrations (>1 mg/mL), as previously suggested (5).

Because the changes in the SAXS patterns of the OCP^R could be attributed to structural changes, and not oligomeric state changes, we next applied ab initio bead modeling to obtain more information about the global structure of OCP^R (20, 21). The filtered shape envelope calculated from the SAXS profile of OCP^O was consistent with the shape and size of the OCP monomer in the crystal structure (Fig. 1*D*) (5). The envelope for OCP^R showed a narrower and longer shape, in which the isolated NTD and CTD of the OCP could be readily fit (Fig. 1*E*). To obtain more structural information on OCP^R, we applied the program Coral (22), which uses iterative rigid body modeling, with the aim of generating a model consistent with experimental SAXS data. The positions of the NTD and CTD of the OCP were treated as isolated rigid bodies, and the N/C-terminal extensions and interdomain linker sequences were added as flexible residues. Although the relative orientation of the two domains varied, the resulting models of the OCP^R were in good agreement with the experimental SAXS profile, with the lowest χ value of 2.59 (Fig. S4 *C* and *D*). In contrast, Coral models sampling different linker and N/C-terminal extensions, without allowing NTD and CTD separation, resulted in very poor fits to the SAXS data (χ > 11). These data constitute, to our knowledge, the first coarse-grained/low resolution view of the overall organization of OCP^R, demonstrating that the two domains fully dissociate upon photoactivation.

Local Structural Changes upon Photoactivation of the OCP as Observed by XF-MS and HDX-MS. With XF-MS, microsecond X-ray pulses ionize both bulk and bound water rapidly and isotropically to generate hydroxyl radicals in situ, which then react with proximal residues to yield stable modification products (13, 23). X-ray radiolysis resulted in reproducible side-chain modifications in OCP^O and OCP^R samples without any significant structural perturbation, as evaluated by UV absorption and SEC-multiangle light scattering (MALS) (Fig. S5*A*). Postirradiation, bottom-up liquid chromatography (LC)-MS analysis using trypsin and Glu-C digestion

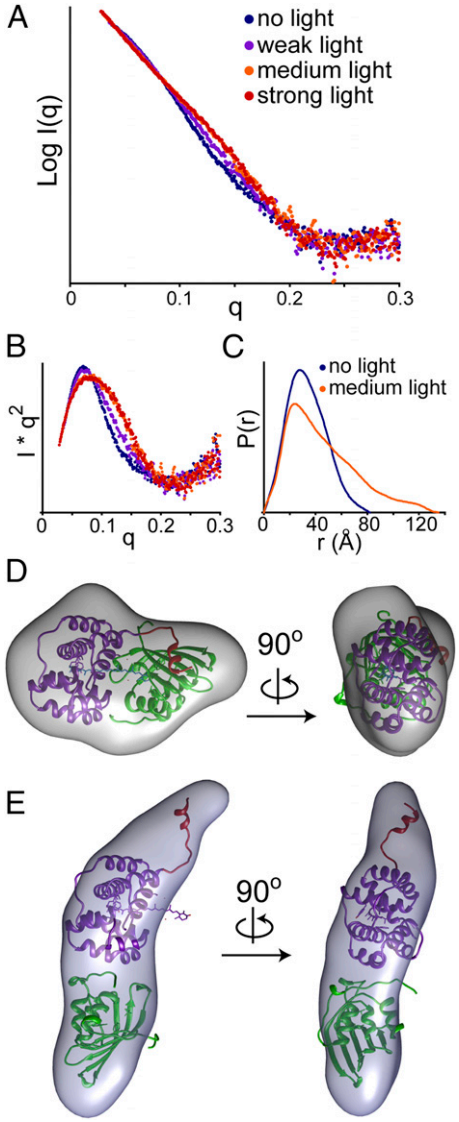

Fig. 1. Global structural changes in the OCP upon activation monitored by SAXS. (*A*) SAXS data for OCP in the absence of light (blue), weak illumination (purple), medium illumination (orange), and strong illumination (red) (see *SI Methods* for specific illumination levels). Guinier plots are shown in Fig. S3*E*. Kratky plots (*B*) and corresponding distance distribution plots (*C*) of the scattering data are shown with the same coloring as in *A*. Ab initio bead reconstructions (gray volumes) are shown for OCP in the absence of light (*D*) and under medium illumination (*E*) using GASBOR (20). Similar results were obtained using DAMMIN, another bead modeling algorithm (Fig. S4 *A* and *B*) (21). (*D*) A monomer of OCP^O from the crystal structure is docked into the volume envelope with the far N-terminal helix (red), N-terminal domain (NTD; purple), and C-terminal domain (CTD; green) (PDB ID code 3MG1) (5). (*E*) The two domains of OCP along with the N-terminal helix were modeled to approximate the volume envelope of OCP^R. The (nontranslocated) carotenoid is shown in sticks.

generated greater than 94% sequence coverage. A progressive increase in the hydroxyl radical dose resulted in residue-specific dose–response plots and provided side chain-specific hydroxyl radical reactivity rates (Fig. S5*B* and Table S5). The rate of side-chain labeling is governed by both the intrinsic reactivity of the amino acid and the solvent accessibility to the side-chain. However, the ratio of the measured reactivity rates for the same residues in the OCP^O vs. OCP^R gave a ratiometric account of the change in accessibility, which was independent of the intrinsic side-chain reactivity (Fig. 2*A*).

HDX-MS, in contrast, uses the natural exchange of protons at backbone amide positions to probe amide proton accessibility (14, 15). Amides involved in hydrogen bonds through stable secondary structure, or that are substantially solvent-occluded, exchange much slower than accessible ones. Pepsin digestion yielded 116 observable fragments, resulting in a net sequence coverage of 98% (Fig. S6*A*). Differences in amide exchange between OCP^o and OCP^R are summarized in Fig. 3. Additional controls were performed to ensure that the light-activated OCP measured by HDX-MS was fully activated OCP^R and that the level of continuous illumination did not damage the protein (Fig. S6 *B* and *C*).

We observed large increases in solvent accessibility by XF-MS in two regions of the protein: first, at the major interface between the NTD-CTD and, second, at the minor interface of the N-terminal helix and CTD (Fig. 2) (5). At the major interface, the largest increase (10-fold) was observed at the conserved NTD residue R155, which forms a salt bridge with E244 on the CTD in the OCP^O (4, 5). We also observed 2- and 1.5-fold increases at absolutely conserved residues P276-W277-Y278 and the moderately conserved M284, respectively. All of these residues are involved in the stabilization of the carotenoid in the major interface (4, 5, 9). In addition, residue W277 H-bonds with N104 on the NTD in the OCP^O (5, 10). Upon photoactivation to OCP^R, the NTD peptide 97–106 showed a cluster of modifications at Y98-W101-P103 that resulted in an overall twofold increase in accessibility. By HDX-MS, residues 241–248 proximal to the major interface showed increased accessibility in OCP^R. In contrast, the NTD helix αI, containing R155, remained protected from exchange upon photoactivation (Fig. 3) and the peptides within NTD helices αF and αG, which include N104, and the CTD β3 sheet, which includes W277, showed only minor changes in the deuterium exchange kinetics. Together, these results suggest that a disruption of the side-chain interactions at the major interface, but without measurable local unfolding of secondary structure (helices), leads to formation of OCP^R.

At the minor interface, NTD residues A8–R9 and 13–22 on the loop joining αA to αB showed a significant increase in accessibility in OCP^R relative to OCP^O by XF-MS, commensurate with the corresponding residues V301-A302-I303 on the surface of the β-sheet facing helix αA. Previous chemical footprinting experiments have also shown increased access to the minor interface, suggesting helix dissociation (11). By HDX-MS, large changes were also observed within the N-terminal helix (residues 2–18), which became completely exchanged within 3 s in OCP^R. This rapid exchange shows that the N-terminal helix (αA) not only dissociates from the CTD but becomes disordered upon photoactivation (Fig. 3 and Fig. S6*D*). The unfolding of this helix is consistent with the slight loss of helical structure predicted by comparison of the far-UV CD spectrum of OCP^R versus that of OCP^O (Table S3). Interestingly, even in OCP^O, this helix exchanges considerably faster than other helical segments, suggesting that this region is somewhat dynamic and only loosely associated with the CTD in the OCP^O. Additionally, HDX-MS also showed that residues 19–31 adjacent to the N-terminal helix become less protected from exchange in OCP^R (Fig. 3). The combination of CD and HDX-MS demonstrates that activation of the OCP results in disruption of the minor interface, the interaction between the N-terminal α-helix and the solvent-exposed β-sheet of the CTD, via the unfolding of the αA (the N-terminal helix). The critical role of the αA helix in OCP photochemistry and function is consistent with a recent mutational analysis that implicated changes in this helix as important to the interaction of the OCP with the PB and the FRP (24). A similar disruption of a helix:domain interaction upon activation was observed in other photoactive proteins, including PYP, BLUF, and LOV (5, 10). BLUF and LOV domain β-scaffolds are well known for their involvement in both intra- and interprotein interactions (25), and we note that previous in silico docking

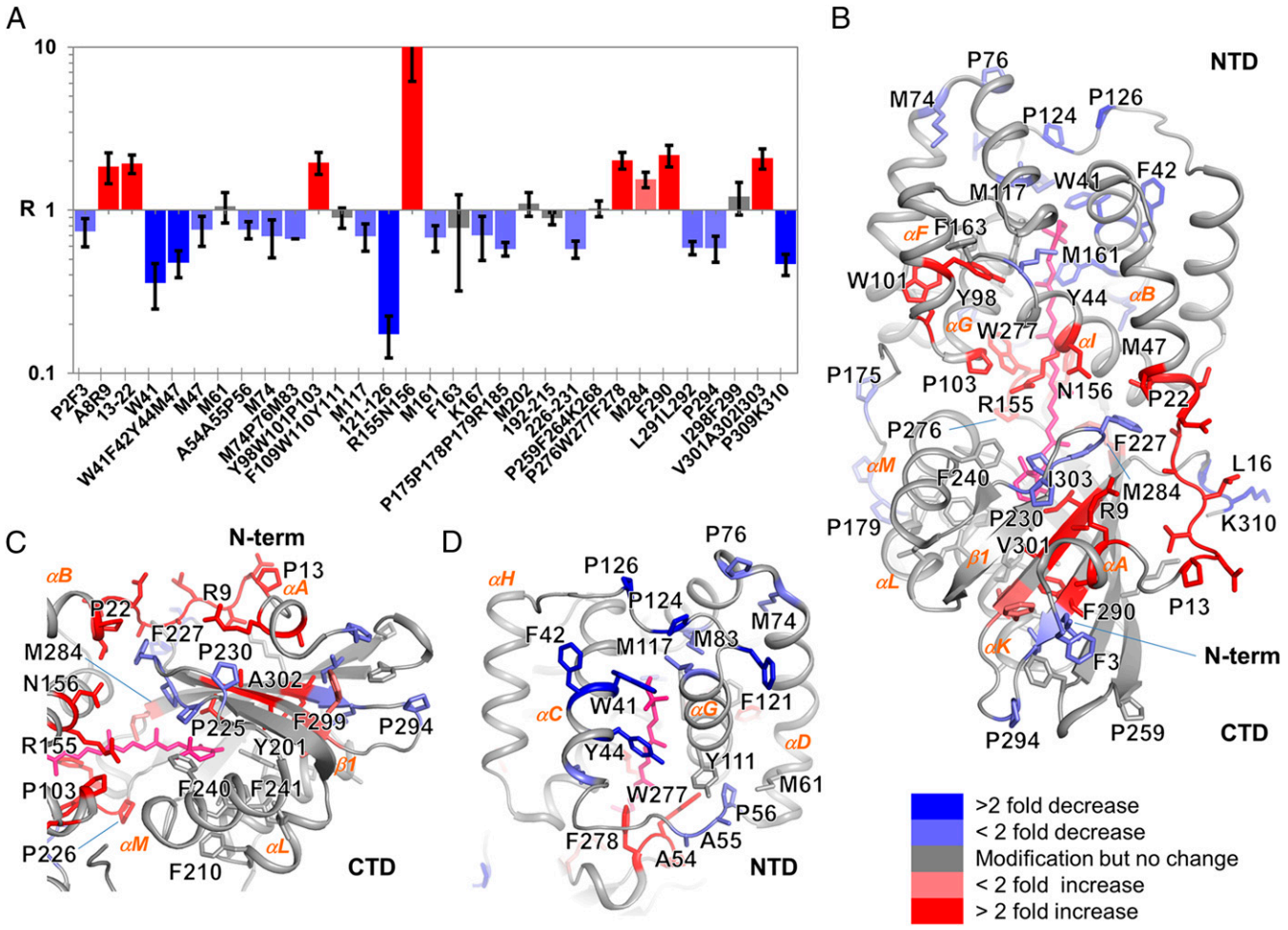

Fig. 2. Local structural changes in the OCP upon activation monitored by XF-MS. (*A*) Solvent accessibility changes in response to photoactivation measured by the ratio (R) of hydroxyl radical reactivity rates for residues obtained from the dose–response plot (Fig. S5*B*). The rate for each site indicated is summarized in Table S5. The coloring indicates changes in rates of modifications upon transition from OCP^O to OCP^R. Error bars represent the SE from three independent measurements. (*B*) Modified residues are represented by sticks on the X-ray crystal structure of OCP^O (PDB ID code 3MG1) (5). The carotenoid is shown in pink sticks. Color codes as in *A* indicate the changes in solvent accessibility upon photoactivation. (*C*) Solvent accessibility changes at the major and minor interface, showing possible destabilization at several interdomain H-bonding and ionic interaction sites. The color codes are the same as in *A*. (*D*) Solvent accessibility changes in the NTD, showing possible stabilization of the shifted carotenoid by conserved aromatics residues, methionine residues, and the loop joining the two four-helix bundles of the NTD. The color codes are the same as in *A*.

experiments between the CTD of the OCP and the FRP implicated β-scaffold residues (including V232, D220, and F299) in the CTD–FRP interaction (8). Accordingly, disruption of the minor interface seems to mediate both an intraprotein (domain dissociation) response and a putative interprotein interaction (with the FRP) that collectively control OCP's photoprotective function.

Local Structural Changes in the Carotenoid Pocket in the OCP upon Light Activation. The recently reported crystal structure of a constitutively active NTD [*Synechocystis* "red carotenoid protein" (RCP) expressed in and isolated from *Escherichia coli*] revealed a 12-Å translocation of the carotenoid into a previously unknown binding configuration in the NTD (9). Additional evidence for light-dependent carotenoid translocation was provided by mutational analysis and XF-MS analysis of carotenoid binding residues in *E. coli*-expressed OCP (binding a mixture of ECN and CAN). Our results support carotenoid translocation in *Synechocystis*-expressed OCP-ECN after photoactivation (Fig. 2): a greater than twofold decrease in solvent accessibility at residue cluster W41-Y42-Y44 in the NTD was observed concomitantly with a greater than twofold increase in solvent accessibility in CTD residue cluster P276-W277-F278, consistent with previously reported results (9). In this study, complementary HDX-MS data on OCP-ECN showed that, whereas some regions are moderately less protected from exchange in OCP^R, the local secondary structure remains largely intact near these carotenoid-binding residues. The combined XF- and HDX-MS data thus solidify the assignment of reciprocal solvent accessibility changes at these sidechains to a reconfiguration of carotenoid-sidechain interactions. Similar reciprocal changes are observed in the light-dependent XF-MS data for carotenoid binding residues in the NTD of OCP-ECN (less than twofold accessibility decrease at M47, M74-P76-M83, and M117) and CTD (less than twofold accessibility increase at M284 and F290). Notably, the OCP^O carotenoid-binding residue M202, which is buried in the hydrophobic core of the CTD, showed no light dependent change in accessibility.

We obtained previously unidentified evidence supporting carotenoid translocation at the linker region (residues 120–131), which connects the two four-helix bundles of the NTD between helices αG and αH. XF-MS showed the largest decrease (greater than fivefold) in accessibility at the NTD residue cluster F121-P124-P126 after photoactivation. HDX-MS data were consistent with

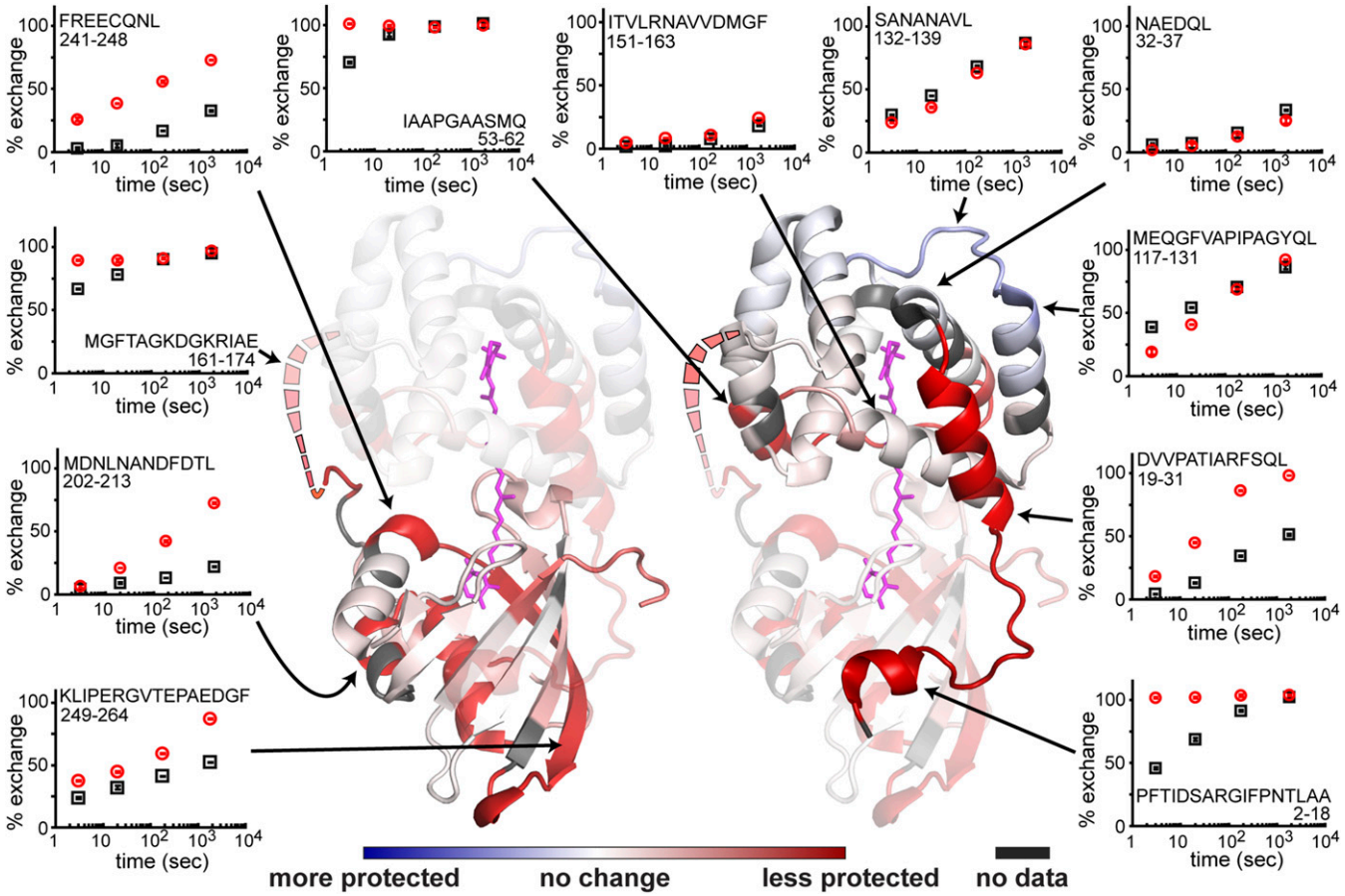

Fig. 3. Local structural changes in the OCP upon light activation as measured by HDX-MS. The changes in solvent accessibility upon light activation are plotted on the OCP crystal structure (PDB ID code 3MG1) (5) showing regions becoming less protected from exchange (red) and more protected from exchange (blue). The carotenoid is shown in magenta sticks. Residues 164–170, not modeled in the crystal structure, are shown as dashed lines. Individual exchange plots for peptides of interest in OCP^O (black squares) and OCP^R (red circles) are shown on the periphery with their corresponding location in the structure indicated by arrows. Exchange data reflect the average from duplicate measurements with error bars showing the SD. Exchange plots for all observed peptides are shown in Fig. S6*D*.

these results because the area around the αG-αH was the only region that was more protected from exchange in OCP^R (Fig. 3). Based on the structure of the isolated NTD (9), the increased protection is likely attributable to the ligand shifting into direct contact with the loop and thereby stabilizing the local structure in this region (Fig. 2*D*).

We observed reciprocal solvent accessibility changes in two structurally proximal regions at the major interface: first, in the loop joining β1 and αM in the CTD (P225-P226-F227 & P230; 1.7-fold decrease) and adjacent residues in the NTD (R9, P22, and N156; twofold increase) (Fig. 2*C*); second, in the loop joining αC and αD, which joins the two four-helix bundles in NTD (A54-A55-P56; 1.3-fold decrease), and the adjacent residue in CTD (W277; twofold increase) (Fig. 2*D*). Similar reciprocal changes were previously described for a membrane-embedded helix and proposed to involve helix reorientation as well as movement of internal water (26). In the *Synechocystis* OCP, the residues involved in this reciprocal interaction are highly conserved and may play an important role in structural stabilization of the hydrophobic core of the CTD after the carotenoid translocation as well as its stabilization in NTD.

In contrast, relatively few changes upon illumination were observed in the accessibility of residues surrounding the carotenoid in the CTD. As noted above, HDX-MS showed that, with the exception of the αA-helix, the secondary structure remains largely intact within OCP^R. Side-chains located on helices αK and αL, which project toward the core of the CTD (peptide 192–215), showed detectable modification in both OCP^O and OCP^R but did not undergo any change in accessibility. Residues Y201 and W288 (no modification) were absolutely conserved and participated in H-bonding to the keto group of the carotenoid in OCP^O (5). Residue F240, projecting toward the β-ionone ring of the carotenoid, and F241, projecting toward the core of the CTD, showed no modification in either OCP^O or OCP^R. Collectively, these results suggest that no major structural changes occur within the carotenoid binding pocket of the CTD upon photoactivation. The translocation of the carotenoid into the NTD upon photoactivation presumably generates a void space in the CTD, and the protection from hydroxyl radical-mediated modification may be explained by the loop joining β1 and αM, limiting the accessibility of the CTD core. The decrease in the accessibility of the loop residues (P225-P226-F227 and P230) is consistent with its capping of the CTD in OCP^R.

The Role of Bound Water and H-Bonding Networks in Carotenoid-to-Protein Signal Propagation. It is known that bound water molecules are important for protein structural stabilization, ligand binding, and conformational changes (27–29). XF-MS generates hydroxyl radicals by activating bulk as well as protein-bound water, which can react directly with proximal side-chains (13, 30). In contrast to bulk water, protein-bound water (identified by

X-ray crystallography) shows a longer residence time in solution and facilitates a significantly higher yield of hydroxyl radical modifications at reactive residues (23, 31). XF-MS has been used to probe the positions of internal water molecules, changes in the H-bonding networks involving bound water, and the dynamic role of internal water in hydrophobic cavities inside protein cores (23, 26, 31–33). In addition to carotenoid translocation (9), our data demonstrate two other structural changes upon photoactivation of the OCP: unfolding and release of the N-terminal helix from the CTD surface and complete dissociation of the NTD and CTD. Our XF-MS analysis detects associated solvent accessibility changes at the functionally important side-chains in these regions that are in close proximity to the bound water. Accordingly, it is plausible that signal propagation occurs from the light-activated carotenoid to the protein surface via internal hydrogen bonding networks and involves bound water molecules.

Comparison of the crystal structures of *Synechocystis* and *Arthrospira maxima* OCP^O reveals three clusters of water molecules in both structures at the major and minor interfaces (Fig. 4); these waters are conserved and/or are within 0.5 Å of each other in both crystal structures (Fig. S1 and Table S6). Waters HOH1020 and 1125 are at the center of two clusters of water molecules (labeled 1 and 2) at the major interface within 3.9 Å of the carotenoid (Fig. 4 *A* and *B*, Fig. S1, and Table S6). R155, which participates in a salt bridge between the NTD and CTD, and which plays an important role in interaction with the phycobilisome during energy dissipation (12), is associated with water cluster 1, which includes HOH1020 (Fig. 4 and Fig. S1*F*). These water

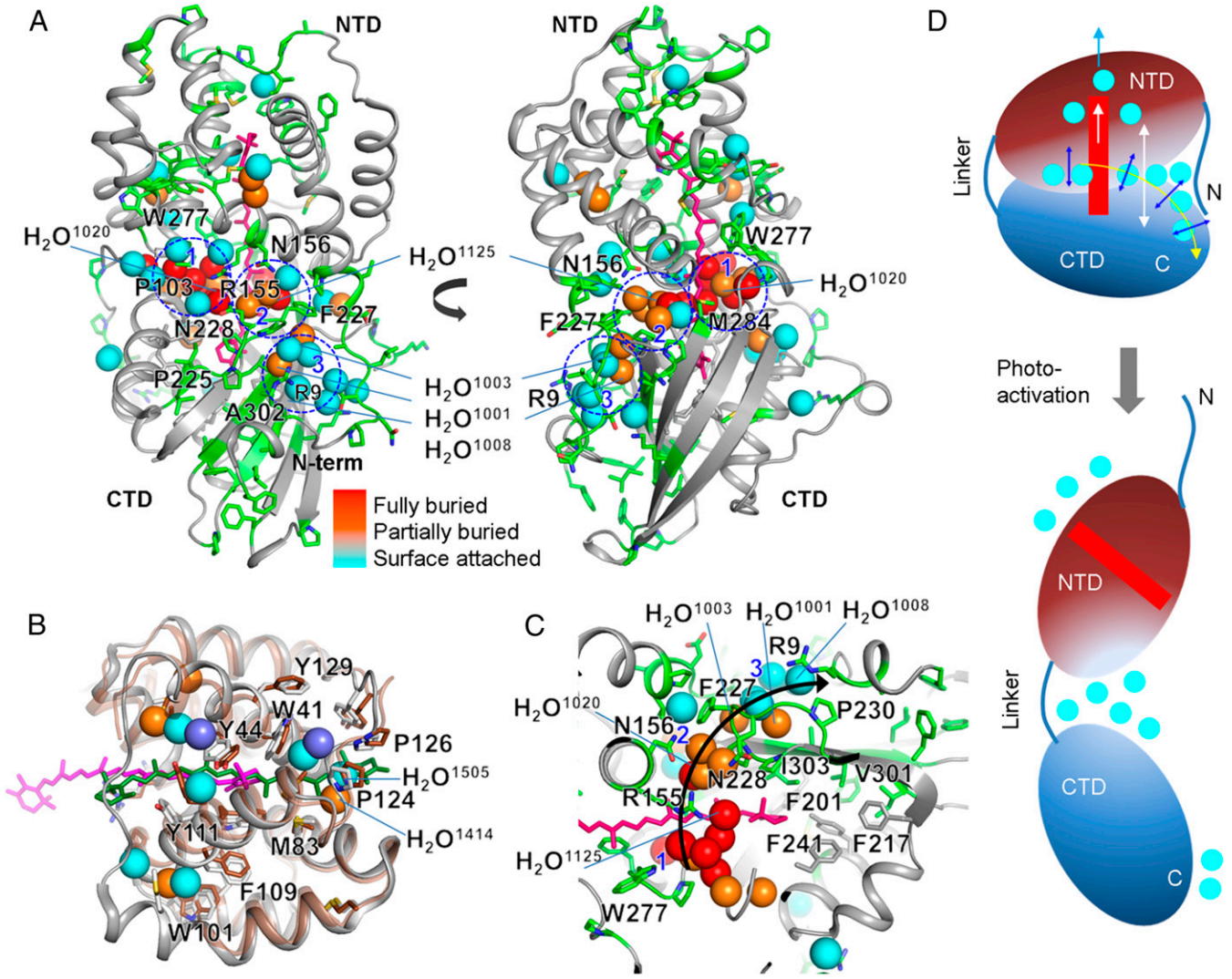

Fig. 4. Water network for carotenoid signaling in OCP. (*A*) Modified residues and the carotenoid are represented by green and pink sticks, respectively, on the X-ray crystal structure of OCP^O from *Synechocystis* (PDB ID code 3MG1). The spheres represent water molecules, which are either conserved (labeled) or located at approximately the same position (within 0.5 Å) in both the crystal structure of *A. maxima* (4) and *Synechocystis* OCP (5). The coloring of the waters indicates their depth from the surface of the OCP (see Fig. S1 *C–E* for additional details). Three major water clusters, at the minor and major interfaces, are marked by blue dashed lines and numbered. These waters potentially form internal H-bonding contacts with side chains, amide backbone, and other water molecules (Fig. S1*F* and Table S6). Residues that undergo the highest degree of solvent accessibility change and are important for the H-bonding network at the major and minor interface are labeled. (*B*) Superimposed structure of the constitutively active RCP (protein in brown, carotenoid in green, buried water as violet spheres) (9) and *Synechocystis* OCP^O (gray, carotenoid in pink, conserved and buried water colored as in *A*) (5). Residues that are proposed to stabilize the carotenoid in the activated state are labeled. (*C*) Proposed signal propagation pathway from the carotenoid through the water-side chain H-bonding network to the protein surface that facilitates carotenoid shift, dissociation of NTD-CTD, and detachment of the N-terminal helix from CTD. (*D*) Schematic of the OCP^O and OCP^R showing regions with the largest conformational rearrangement associated with the change in H-bonding network and water rearrangements.

molecules participate in a constellation of residue–water interactions: R155-HOH1151-W277, R155-HOH1200-HOH1044-S102/P103, W277-N104-HOH1044/HOH1200-R155, and T275/P276-HOH1020. As noted above, most of these conserved residues showed large increases in accessibility upon photoactivation, implying a concomitant change in the water–protein network after domain separation. Also at the major interface, water cluster 2 connects M284, P226, F227, and N156, all of which undergo changes in side-chain accessibility upon photoactivation. Water cluster 3, at the minor interface, consists of structurally conserved and partially buried water molecules (HOH1001, HOH1003, and HOH1008) and connects A302-I303 of β5 to R9 of the N-terminal helix αA, and F227-P226 of the loop joining β1 and αM (Fig. 4*C*) facing the minor interface. In addition, residues F227–P226 and the adjacent Q228 of the same loop are directly connected to water cluster 2 at the major interface. These water clusters and adjacent residues may form a pathway (water cluster 1 > R155-N156 of NTD > water cluster 2 > F227/P226 of CTD > water cluster 3) (Fig. 4*C*) and may even provide a means of communication from the carotenoid binding pocket to the surface of the protein, while concomitantly playing a role in domain dissociation. The alternate and reciprocal (increase-decrease-increase) accessibility along the major interface, the loop joining β1 and αM, and the minor interface indicate a continuous movement/displacement of water molecules, as well as reorganization of the H-bonding network that drives domain dissociation after the carotenoid translocation.

To summarize, the combination of structural MS methods with CD and SAXS provides both local and global structural insight into the structure of the OCP^R, which has remained recalcitrant to crystallization. We have defined the specific changes in interactions at the major NTD–CTD interface, and, critically, SAXS results have confirmed that complete separation of the NTD and CTD occurs in the OCP^R form. Domain separation is predicated on carotenoid translocation, as well as unfolding of the loosely associated N-terminal helix and its dissociation from the CTD (Fig. 4*D*). We also demonstrate that a change in the oligomeric state (i.e., dimerization) is not required for photoactivation and that the secondary structural content in each individual domain remains largely intact during the photoactivation process, with the exception of the α1-helix. Collectively, these results offer insight that will aid efforts to investigate the interactions of OCP^R with its binding partners in the course of regulating photoprotection, such as cross-linking studies (18) and in silico modeling of protein–protein interactions (8, 9, 18). These findings will also enable more accurate modeling of the OCP–PB complex, a major step in delineating the mechanisms of the complete photoprotective system.

Methods

OCP was purified from an OCP-overexpressing mutant strain of *Synechocystis* PCC 6803 (a gift of Diana Kirilovsky, Commissariat à l'Energie Atomique, Institut de Biologie et Technologies de Saclay, Gif-sur-Yvette, France) using a procedure described previously (5, 7) with modifications described in *SI Methods*. SAXS measurements were conducted on beamline 4-2 at the Stanford Synchrotron Radiation Laboratory, with an online SEC-SAXS setup with varying levels of blue LED illumination immediately before X-ray exposure. OCP^O was converted to OCP^R by blue LED illumination on ice before XF-MS measurements. Deuterium exchange reactions were conducted either in the absence of light or under constant illumination of the blue LED. XF-MS (13) measurements were made at the Advanced Light Source beamline 5.3.1 (30). Extensive details of the data collection for all methods are provided in *SI Methods*.

ACKNOWLEDGMENTS. We thank Tsutomu Matsui and the support staff at the Stanford Synchrotron Radiation Lightsource (SSRL) for assistance with SAXS data collection, as well as Rich Celestre for help with data collection on Advanced Light Source beamline 5.3.1. This work was supported by National Institutes of Health (NIH) Grants F32-GM097805 and R01-GM099989 (to K.K.L. and M.G.) and Office of Science of the US Department of Energy (DOE) Grant DE-FG02-91ER20021 (to C.A.K., E.G.P., and R.L.L.). This work was supported in part by NIH Grant P30EB009998. The Advanced Light Source at Lawrence Berkeley National Laboratory is supported by the Director, Office of Science, Office of Basic Energy Sciences, US DOE under Contract DE-AC02-05CH11231. The SSRL Structural Molecular Biology Program is supported by the Department of Energy Office of Biological and Environmental Research and by NIH National Institute of General Medical Sciences Grant P41GM103393 and National Center for Research Resources Grant P41RR001209. This research used resources of the Joint BioEnergy Institute supported by the Office of Science, Office of Biological and Environmental Research, US DOE under contract DE-AC02-05CH11231.

1. Müller P, Li XP, Niyogi KK (2001) Non-photochemical quenching: A response to excess light energy. *Plant Physiol* 125(4):1558–1566.
2. Pascal AA, et al. (2005) Molecular basis of photoprotection and control of photosynthetic light-harvesting. *Nature* 436(7047):134–137.
3. Niyogi KK, Truong TB (2013) Evolution of flexible non-photochemical quenching mechanisms that regulate light harvesting in oxygenic photosynthesis. *Curr Opin Plant Biol* 16(3):307–314.
4. Kerfeld CA, et al. (2003) The crystal structure of a cyanobacterial water-soluble carotenoid binding protein. *Structure* 11(1):55–65.
5. Wilson A, et al. (2010) Structural determinants underlying photoprotection in the photoactive orange carotenoid protein of cyanobacteria. *J Biol Chem* 285(24):18364–18375.
6. Leverenz RL, et al. (2014) Structural and functional modularity of the orange carotenoid protein: Distinct roles for the N- and C-terminal domains in cyanobacterial photoprotection. *Plant Cell* 26(1):426–437.
7. Wilson A, et al. (2008) A photoactive carotenoid protein acting as light intensity sensor. *Proc Natl Acad Sci USA* 105(33):12075–12080.
8. Sutter M, et al. (2013) Crystal structure of the FRP and identification of the active site for modulation of OCP-mediated photoprotection in cyanobacteria. *Proc Natl Acad Sci USA* 110(24):10022–10027.
9. Leverenz RL, et al. (2015) A 12 Å carotenoid translocation in a photoswitch associated with cyanobacterial photoprotection. *Science* 348(6242):1463–1466.
10. Kirilovsky D, Kerfeld CA (2013) The Orange Carotenoid Protein: A blue-green light photoactive protein. *Photochem Photobiol Sci* 12(7):1135–1143.
11. Liu H, et al. (2014) Mass spectrometry footprinting reveals the structural rearrangements of cyanobacterial orange carotenoid protein upon light activation. *Biochim Biophys Acta* 1837(12):1955–1963.
12. Wilson A, et al. (2012) The essential role of the N-terminal domain of the orange carotenoid protein in cyanobacterial photoprotection: Importance of a positive charge for phycobilisome binding. *Plant Cell* 24(5):1972–1983.
13. Xu G, Chance MR (2007) Hydroxyl radical-mediated modification of proteins as probes for structural proteomics. *Chem Rev* 107(8):3514–3543.
14. Konermann L, Pan J, Liu YH (2011) Hydrogen exchange mass spectrometry for studying protein structure and dynamics. *Chem Soc Rev* 40(3):1224–1234.
15. Marcsisin SR, Engen JR (2010) Hydrogen exchange mass spectrometry: What is it and what can it tell us? *Anal Bioanal Chem* 397(3):967–972.
16. Putnam CD, Hammel M, Hura GL, Tainer JA (2007) X-ray solution scattering (SAXS) combined with crystallography and computation: Defining accurate macromolecular structures, conformations and assemblies in solution. *Q Rev Biophys* 40(3):191–285.
17. Sreerama N, Woody RW (2000) Estimation of protein secondary structure from circular dichroism spectra: Comparison of CONTIN, SELCON, and CDSSTR methods with an expanded reference set. *Anal Biochem* 287(2):252–260.
18. Zhang H, et al. (2014) Molecular mechanism of photoactivation and structural location of the cyanobacterial orange carotenoid protein. *Biochemistry* 53(1):13–19.
19. Fischer H, de Oliveira Neto M, Napolitano HB, Craievich AF, Polikarpov I (2010) The molecular weight of proteins in solution can be determined from a single SAXS measurement on a relative scale. *J Appl Cryst* 43:101–109.
20. Svergun DI, Petoukhov MV, Koch MH (2001) Determination of domain structure of proteins from X-ray solution scattering. *Biophys J* 80(6):2946–2953.
21. Svergun DI (1999) Restoring low resolution structure of biological macromolecules from solution scattering using simulated annealing. *Biophys J* 76(6):2879–2886.
22. Petoukhov MV, et al. (2012) New developments in the ATSAS program package for small-angle scattering data analysis. *J Appl Cryst* 45(Pt 2):342–350.
23. Gupta S, D'Mello R, Chance MR (2012) Structure and dynamics of protein waters revealed by radiolysis and mass spectrometry. *Proc Natl Acad Sci USA* 109(37):14882–14887.
24. Thurotte A, et al. (2015) Regulation of Orange Carotenoid Protein activity in cyanobacterial photoprotection. *Plant Physiol* 169(1):737–747.
25. Zoltowski BD, Gardner KH (2011) Tripping the light fantastic: Blue-light photoreceptors as examples of environmentally modulated protein-protein interactions. *Biochemistry* 50(1):4–16.
26. Gupta S, et al. (2014) Visualizing the kinetic power stroke that drives proton-coupled zinc(II) transport. *Nature* 512(7512):101–104.
27. Breiten B, et al. (2013) Water networks contribute to enthalpy/entropy compensation in protein-ligand binding. *J Am Chem Soc* 135(41):15579–15584.
28. Bhat TN, et al. (1994) Bound water molecules and conformational stabilization help mediate an antigen-antibody association. *Proc Natl Acad Sci USA* 91(3):1089–1093.
29. Ball P (2008) Water as an active constituent in cell biology. *Chem Rev* 108(1):74–108.

30. Gupta S, Celestre R, Petzold CJ, Chance MR, Ralston C (2014) Development of a microsecond X-ray protein footprinting facility at the Advanced Light Source. *J Synchrotron Radiat* 21(Pt 4):690–699.
31. Angel TE, Gupta S, Jastrzebska B, Palczewski K, Chance MR (2009) Structural waters define a functional channel mediating activation of the GPCR, rhodopsin. *Proc Natl Acad Sci USA* 106(34):14367–14372.
32. Gupta S, et al. (2010) Conformational changes during the gating of a potassium channel revealed by structural mass spectrometry. *Structure* 18(7):839–846.
33. Frankel LK, et al. (2013) Radiolytic mapping of solvent-contact surfaces in Photosystem II of higher plants: Experimental identification of putative water channels within the photosystem. *J Biol Chem* 288(32):23565–23572.
34. Wilson A, Punginelli C, Couturier M, Perreau F, Kirilovsky D (2011) Essential role of two tyrosines and two tryptophans on the photoprotection activity of the Orange Carotenoid Protein. *Biochim Biophys Acta* 1807(3):293–301.
35. Britton G, Liaaen-Jensen S, Pfander H, eds (2004) *Carotenoids Handbook* (Birkhäuser, Basel).
36. Greenfield NJ (2006) Using circular dichroism spectra to estimate protein secondary structure. *Nat Protoc* 1(6):2876–2890.
37. Smolsky IL, et al. (2007) Biological small-angle X-ray scattering facility at the Stanford Synchrotron Radiation Laboratory. *J Appl Cryst* 40:s453–s458.
38. Petoukhov MV, Konarev PV, Kikhney AG, Svergun DI (2007) ATSAS 2.1: Towards automated and web-supported small-angle scattering data analysis. *J Appl Cryst* 40: s223–s228.
39. Konarev PV, Volkov VV, Sokolova AV, Koch MHJ, Svergun DI (2003) PRIMUS: A Windows PC-based system for small-angle scattering data analysis. *J Appl Cryst* 36(5): 1277–1282.
40. Svergun DI (1992) Determination of the regularization parameter in indirect-transform methods using perceptual criteria. *J Appl Cryst* 25:495–503.
41. Kozin MB, Svergun DI (2001) Automated matching of high- and low-resolution structural models. *J Appl Cryst* 34:33–41.
42. Volkov VV, Svergun DI (2003) Uniqueness of ab-initio shape determination in small-angle scattering. *J Appl Cryst* 36:860–864.
43. Pettersen EF, et al. (2004) UCSF Chimera: A visualization system for exploratory research and analysis. *J Comput Chem* 25(13):1605–1612.
44. Zhang Z, Zhang A, Xiao G (2012) Improved protein hydrogen/deuterium exchange mass spectrometry platform with fully automated data processing. *Anal Chem* 84(11): 4942–4949.
45. Guttman M, Weis DD, Engen JR, Lee KK (2013) Analysis of overlapped and noisy hydrogen/deuterium exchange mass spectra. *J Am Soc Mass Spectrom* 24(12): 1906–1912.